Earth and Space Science

RESEARCH ARTICLE
10.1029/2020EA001631

Special Section:
Results from 10 Years of UAVSAR Observations

Comparison of Surface Subsidence Measured by Airborne and Satellite InSAR Over Permafrost Areas Near Yellowknife Canada

Xingyu Xu[1], Lin Liu[1], Kevin Schaefer[2], and Roger Michaelides[3]

[1]Earth System Science Programme, Faculty of Science, The Chinese University of Hong Kong, Hong Kong, China, [2]National Snow and Ice Data Center, Cooperative Institute for Research in Environmental Sciences, University of Colorado at Boulder, Boulder, CO, USA, [3]Department of Geophysics, Colorado School of Mines, Golden, CO, USA

Key Points:

- We compare the seasonal subsidence derived from airborne and satellite InSAR measurements
- Two UAVSAR interferograms are self-consistent while a significant deviation exists between the UAVSAR and ALOS2 results
- We discuss the difference and the potential combination use of spaceborne and airborne InSAR to improve subsidence measurements over permafrost regions

Correspondence to:
X. Xu,
xuxingyu@link.cuhk.edu.hk

Citation:
Xu, X., Liu, L., Schaefer, K., & Michaelides, R. (2021). Comparison of surface subsidence measured by airborne and satellite InSAR over permafrost areas near Yellowknife Canada. *Earth and Space Science*, *8*, e2020EA001631. https://doi.org/10.1029/2020EA001631

Received 30 DEC 2020
Accepted 9 MAY 2021

Abstract In addition to spaceborne Interferometric Synthetic Aperture Radar (InSAR), airborne data such as those obtained by the Uninhabited Aerial Vehicle Synthetic Aperture Radar (UAVSAR) have also been utilized to measure surface subsidence in permafrost areas in recent years. Motivated by the integration of multiplatform InSAR data, we generated two UAVSAR interferograms and one Advanced Land Observing Satellite (ALOS)-2 L-band interferogram over a permafrost area near Yellowknife, Canada, then compared the surface subsidence in the thaw seasons of 2017. The correlation coefficient and the root mean square error (RMSE) of subsidence difference are calculated to compare the airborne and spaceborne InSAR measurements. The results demonstrate that the two UAVSAR measurements are self-consistent, with the correlation coefficient between independent airborne measurements ~0.7. While the RMSE of the difference between surface subsidence measured by UAVSAR and ALOS2 is ~2.0 cm, and the correlation coefficients are less than 0.41, that is, a noticeable deviation exists between the UAVSAR and ALOS2 results possibly due to different spatial resolution and the calibration processing of airborne and spaceborne InSAR data. In addition, both UAVSAR and ALOS2 interferograms show larger surface subsidence within taiga needleleaf forest regions than in regions of other biome types (including needleleaf forest, shrubland, and grassland). The results demonstrate that a scheme for the elimination of systematic differences needs to be developed before merging multisource InSAR results. This intercomparison will provide valuable insights for narrowing the gap between radar-based measurements and planning the integration of airborne and satellite InSAR measurements in permafrost environments.

1. Introduction

The ground surface over permafrost regions undergoes seasonal subsidence in summer due to the thawing of the active layer. Permafrost subsidence can result in slope instabilities, destructions of infrastructure and have impacts on local ecosystems and potential increase of greenhouse gas emissions (Hjort et al., 2018; Nauta et al., 2015; Schuur et al., 2015; Strozzi et al., 2018; Turetsky et al., 2020). Seasonal subsidence is also an important parameter to study permafrost status, such as active layer thickness (ALT). The Remotely Sensed Active Layer Thickness (ReSALT) retrieval algorithm has been developed to estimate ALT from measured seasonal subsidence (Liu et al., 2012; Schaefer et al., 2015).

Different methods are used to measure the surface elevation change in the permafrost regions, including traditional in situ mechanical methods (Gruber, 2020; Harris et al., 2007; Mackay & Leslie, 1987), leveling surveys (Mackay & Burn, 2002), and remote sensing techniques such as differential Global Positioning System (GPS) (Streletskiy et al., 2017) and GPS interferometric reflectometry (Hu et al., 2018). In addition, the spaceborne Interferometric Synthetic Aperture Radar (InSAR) technique has been extensively utilized in measuring surface subsidence (Antonova et al., 2018; Beck et al., 2015; Chen et al., 2018; Daout et al., 2017; Liu et al., 2010, 2012) and inferring ALT (Schaefer, Liu & Parsekian, et al., 2015) in permafrost areas owing to its broad spatial coverage, high accuracy, repeat acquisitions, and available data sets. Short et al. (2011) compared the performance of TerraSAR-X, RADARSAT-2, and Advanced Land Observing Satellite (ALOS)-PALSAR interferometry in characterizing surface movement in permafrost environment and found these three sensors show promising applicability of InSAR in monitoring permafrost stability with the L-band SAR performing best in terms of coherence. Wang et al. (2017) also demonstrated the feasibility

and superiority of L-band ALOS PALSAR Interferometry in retrieving ground displacement in the discontinuous permafrost region. Sentinel-1 SAR Interferometry also shows successful application in detecting surface deformation in low-land permafrost areas (Strozzi et al., 2018). These previous studies confirm the viability of using remote sensing InSAR to detect near-surface dynamics of permafrost environments. But the main deficiency in current satellite data for monitoring permafrost is the coarse spatial resolution, with atmospheric effects as well as infrequent observations (Duncan et al., 2020).

Airborne SAR data have also been increasingly employed to detect ground displacement in recent years. The Arctic-Boreal Vulnerability Experiment (ABoVE) airborne campaign, which is carried out by NASA, expands access to observational data for the Arctic and boreal research (Miller et al., 2019). This campaign is aimed at investigating the vulnerability and resiliency of ecosystems to environmental changes in Alaska and western Canada. Aircrafts are equipped with diverse sensors and payloads to collect key measurements of the earth surface. Among them, Uninhabited Aerial Vehicle Synthetic Aperture Radar (UAVSAR), which is an airborne image radar instrument aboard on uninhabited aerial vehicles collecting L-band SAR data, enables effective applications in quantifying and monitoring earth deformation due to earthquakes, volcanic activities, and landslide events (Delbridge et al., 2015, 2016; Donnellan et al., 2014; Fielding et al., 2017; Schaefer, Lu & Oommen, et al., 2015; Schaefer et al., 2016). For characterizing permafrost conditions, the L-band UAVSAR data and the P-band AirMOSS have been used to retrieve soil dielectric constants and ALT in Alaska (Chen et al., 2019). The airborne L-band InSAR system has the potential to measure centimeter-level deformation with flexible temporal and spatial baseline (Cao et al., 2017). UAVSAR measurements with high resolution have been recognized as an effective supplement to satellite data and a valuable technique for improving the spatial coverage and scale of remote sensing in Arctic ecosystems (Beamish et al., 2020).

Since satellite and airborne InSAR measurements have different temporal and spatial resolutions and error sources, they complement each other and can be potentially combined to study permafrost thaw evolution. A few efforts have been devoted to integrating multi-source InSAR measurements. Cao et al. (2017) studied the Slumgullion landslide by combining spaceborne COSMO-SkyMed SAR images and airborne SlimSAR measurements. Their results show a good agreement between the spaceborne and airborne measurements, and they built a three-dimension subsidence model based on these two data sets. There have also been some attempts to integrate ground-based interferometric radar with satellite interferometry in landslide studies (Bardi et al., 2014; Carlà et al., 2018, 2019). However, there still lacks a comparison between satellite remote sensing and airborne measurements over permafrost landscapes to provide quantitative evidence for the existing difference between different platforms. Since airborne and spaceborne InSAR platforms vary in the aspects of employed instruments, imaging geometry, baseline estimation, error sources, and native resolution, cross-comparison of airborne and spaceborne InSAR data sets offer the opportunity for investigating the influence of these different error sources on subsidence measurements. Besides, direct comparison is an important first step toward combining available airborne and satellite observations in monitoring permafrost dynamics. To better utilize the growing airborne InSAR measurements over permafrost regions, it is worth comparing the two types of data sets and quantifying the systematic difference between airborne and spaceborne measured subsidence for improved permafrost characterization. The findings help assess the potential of integrating available airborne and satellite data sets toward a comprehensive understanding of seasonal subsidence in permafrost regions.

In this study, we investigate the difference between airborne and spaceborne InSAR measurements in permafrost studies and discuss potential combination methods. Motivated by the combination of different InSAR measurements, we compare airborne UAVSAR and ALOS2 interferograms over permafrost areas near Yellowknife, Canada. First, we produce interferograms and obtain thaw-season subsidence separately from L-band SAR images taken by UAVSAR and ALOS2. Then, the subsidence maps in the common area obtained from these interferograms are compared in terms of quality, coherence, and spatial pattern. The major differences between UAVSAR and ALOS2 results are analyzed, and the potential combination methods are discussed.

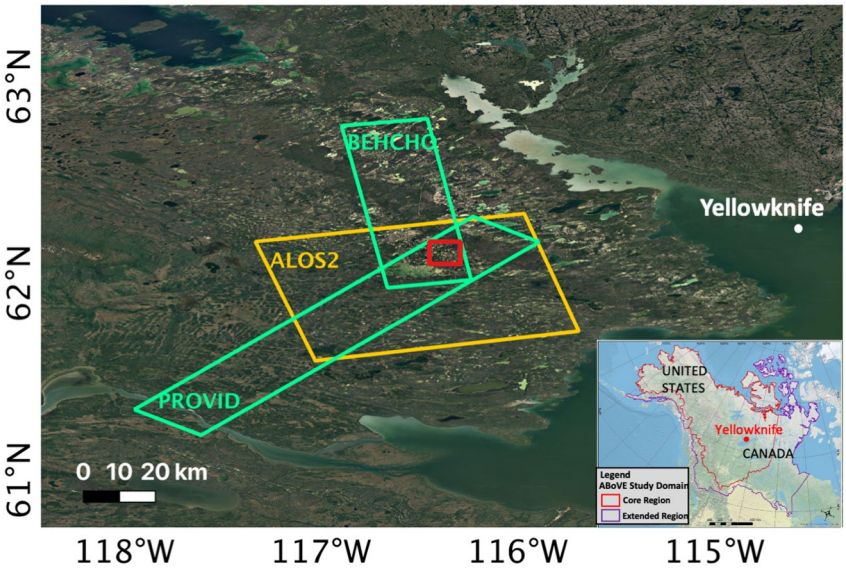

Figure 1. Yellowknife study regions (Google Earth) with interferogram extents outlined in yellow (satellite) and green boxes (airborne UAVSAR) and a common area outlined in red box. The inset shows the ABoVE study domain of the ABoVE program (Miller et al., 2019). ABoVE, Arctic-Boreal Vulnerability Experiment; UAVSAR, Uninhabited Aerial Vehicle Synthetic Aperture Radar.

2. Materials and Methods

The study area, underlain by discontinuous permafrost, is located near Yellowknife in northern Canada, which serves as the base of operations for the Canadian circuit of the ABoVE campaign. A common area with all major water bodies excluded is selected as the focused study area from the overlapped coverage of ALOS2 and UAVSAR scenes in this region (Figure 1). Figure 2 shows the Google Earth image and Canada landcover map version 2015 in this common study area. The main landcover types in the common region include needleleaf forest, taiga needleleaf forest, shrubland, and grassland. A large area of forests transitioned into shrubland and grassland due to the local wildfires in 2011 and 2015 according to the Canadian National Fire Database (https://cwfis.cfs.nrcan.gc.ca/ha/nfdb). There is no obvious difference in subsidence between the fire scars and the surrounding unburned areas perhaps because the surface vegetation grows back after the fire (Brown et al., 2015; Mackay, 1995; Michaelides et al., 2019; Shur & Jorgenson, 2007). Therefore, the influence of fire is not discussed when comparing the interferograms.

2.1. InSAR Data Processing

UAVSAR is an airborne, L-band, fully polarimetric radar mounted to a piloted Gulfstream III aircraft. The nominal flight altitude for UAVSAR is 12,500 m. UAVSAR interferograms are processed by NASA Jet

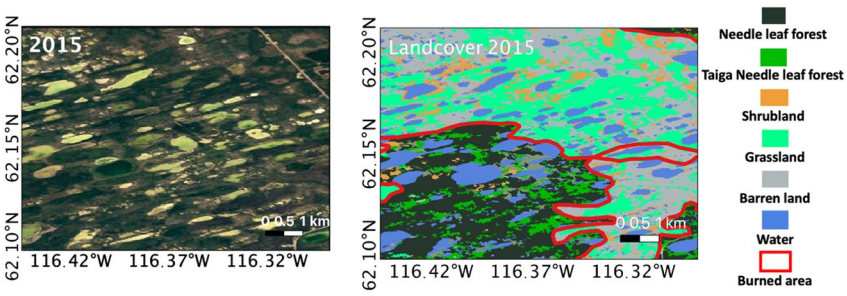

Figure 2. Google Earth image (left) and land cover (right) (https://geoscan.nrcan.gc.ca) in 2015 of the common area outlined in Figure 1.

Table 1
Basic Information of InSAR Observations

Interferogram ID	Time interval (mm.dd)	Incidence angle (deg.)	Range spacing (single-look) (m)	Azimuth spacing (single-look) (m)	Nominal platform altitude (km)
ALOS2-2017	07.13–09.21	28.56–34.03	9.1	5.30	628
UAV-BEHCHO-2017	06.14–09.09	20.12–65.57	1.7	0.6	12.5
UAV-PROVID-2017	06.14–09.09	17.81–65.33	1.7	0.6	12.5

Propulsion Laboratory (JPL) and available online (https://uavsar.jpl.nasa.gov). Considering the aircraft motion caused by air turbulence, motion compensation is an additional required procedure in airborne data processing (Hensley, Michel, et al., 2009; Hensley, Zebker, et al., 2009; Stevens et al., 1995). The motion alignment algorithm was utilized to make the images co-aligned and subsequently generate single look complex (SLC) imagery. The spatial resolution of the SLC imagery is ~1.7 m in range and ~0.6 m in azimuth. Since the Shuttle Radar Topography Mission (SRTM) 1″ and 3″ Digital Elevation Model (DEM) products do not cover areas north of 60°, 30″ SRTM (SRTM30) DEM version 2 (~900 m) was employed to remove the topographic phases from the interferometric phase. After residual baseline correction and co-registration of pair images, wrapped interferograms are formed and established as one of the JPL products. Two interferograms (ID: "BEHCHO" and "PROVID") were both generated using the pair images acquired on June 14 and September 9, 2017, near Yellowknife. The numbers of looks in range and azimuth are 3 and 12, respectively; and the output resolution is 5.0 m in range and 7.2 m in azimuth. The interferograms were then unwrapped using the SNAPHU algorithm (Chen & Zebker, 2002). All UAVSAR products in this analysis were resampled to a 30-m grid using the nearest neighbor resampling.

The satellite data sets utilized are L-band SAR images acquired by ALOS2 Japanese Satellites during the summer of 2017. Two interferograms from ALOS2 satellite scenes were processed with conventional InSAR processing methods using the ISCE software (Rosen et al., 2012). The ALOS2 interferogram is at a 27.3 m by 42.4 m (range/azimuth) resolution (multilooked 3×8 in range/azimuth). To enable direct comparison with the UAVSAR results, 30″ SRTM30 DEM version 2, which has been resampled to 30 m, was adopted to remove topographic effects from ALOS2 interferograms. The basic information of the involved InSAR observations is summarized in Table 1.

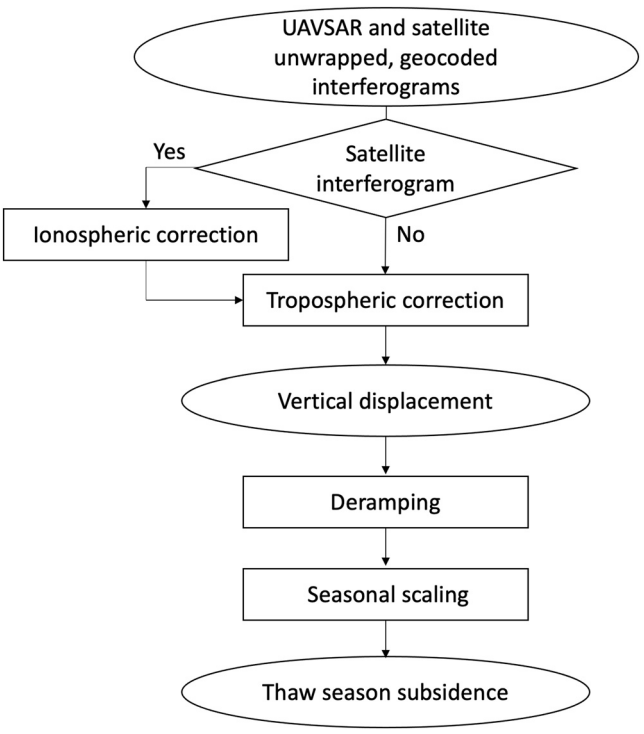

Figure 3. Flowchart of InSAR data post-processing. InSAR, Interferometric Synthetic Aperture Radar.

After the phases were unwrapped and geocoded, a series of post-processing procedures were conducted to eliminate errors from the UAVSAR and ALOS2 interferograms, as illustrated in Figure 3 and detailed below.

2.1.1. Atmospheric Correction

The microwave signals of a spaceborne SAR sensor suffer from both ionospheric delay and tropospheric delay when propagating through the atmosphere, while airborne SAR measurements are only affected by tropospheric delay due to the relatively low flight height of the aircraft (12.5 km). Based on the dispersive character of the ionosphere at microwave frequencies, a split range-spectrum technique can be used to estimate the ionospheric delay suffered by ALOS2 interferogram (Brcic et al., 2010; Fattahi et al., 2017; Gomba et al., 2015; Rosen et al., 2010). In this technique, subband images from two acquisitions are combined to form two subband interferograms and to estimate the dispersive and nondispersive components of the interferometric phase. The dispersive component represents the ionospheric phase delay. This algorithm has been implemented in ISCE and was conducted to remove ionospheric artifacts from the ALOS2 interferogram.

We removed tropospheric noise in both UAVSAR and ALOS2 observations using a boxcar filter on the unwrapped phase (Michaelides

et al., 2021 submitted to the same issue). We assumed the noise occurred at spatial scales of 10 km or larger and the desired subsidence signal occurred at smaller spatial scales of less than 1 km. The boxcar filter calculated a 16-km running smoother across the entire scene representing noise. Subtracting the smoothed phase leaves small-scale subsidence associated with the thawing of the active layer. The propagational errors associated with aircraft motion and incidence angle variations are also assumed to be largely removed through this procedure.

2.1.2. Vertical Displacement and Deramping

Since InSAR measures the phase change along the line-of-sight (LOS) direction during the time interval, it was then converted to vertical displacement under the assumption that ground subsidence is predominantly in the vertical direction:

$$D = \frac{\lambda}{4\pi \cos\theta}\phi \tag{1}$$

where λ is the radar wavelength, θ is the radar incidence angle, and ϕ is the unwrapped interferometric phase in radians.

After atmospheric correction, obvious phase ramps still existed in some interferograms, which might be attributed to the remaining long-wavelength errors. Linear regression was subsequently applied to remove a best-fit ramp from each interferogram.

2.1.3. Seasonal Scaling

Although all the interferograms were obtained during summer, the time intervals between scenes vary from two months to three months and do not exactly span the full thaw season. To make these InSAR results directly comparable, the vertical displacements were then scaled to the thaw-season subsidence. We only considered the surface subsidence due to permafrost thaw without considering other drivers such as thaw consolidation, thermokarst, or erosion effects. Previously the total seasonal subsidence was extrapolated based on the relationship with accumulated degree days of the thaw (ADDT), which required known thaw onsets (Liu et al., 2012). To mitigate the uncertainties introduced by the onset of thaw and gain more stable estimates of seasonal subsidence, a modified approach was applied (Michaelides et al., 2021 submitted to the same issue). This deformation scaling model was constructed based on the Stefan equation which assumed homogeneous soil texture, without considering the lateral changes of heat and water (Stefan, 1891). The model also did not take the influence of complex stratigraphies, hydrology, and late-lying snow into account due to the limited field data, which might lead to bias when estimating seasonal subsidence (Gruber et al., 2020).

$$S = \frac{\sqrt{ADDT_{max}}}{\sqrt{ADDT_2 - ADDT_1}} * D \tag{2}$$

where S is the seasonal subsidence over the entire thaw season, D is the measured subsidence between two scenes. $ADDT_{max}$ is the accumulated degree days of the whole thaw season, $ADDT_1$ and $ADDT_2$ are the accumulated degree days of the thaw for the starting date and end date of time interval, respectively. ADDT is calculated by summing daily temperatures above 0°C at the center of each interferogram. The temperature data used are Daily Surface Weather and Climatological Summaries temperature products available from the Distributed Active Archive Center for Biogeochemical Dynamics (https://daymet.ornl.gov).

Without a reliably identifiable reference pixel, the interferograms were finally referenced by treating the median value of subsidence in the barren land of the common area as zero ground subsidence.

2.2. Comparison of UAVSAR and ALOS2 Measurements

Next, we compared the airborne and satellite InSAR measurements of seasonal subsidence. First, the total seasonal subsidence in the thaw season within barren land was compared between ALOS2 and UAVSAR

Table 2
Mean and Standard Deviation (STD) of Thaw-Season Subsidence at Barren Land Pixels

	Entire interferogram		Common area	
Interferogram ID	Mean (cm)	STD (cm)	Mean (cm)	STD (cm)
ALOS2-2017	0.11	0.83	0.45	1.06
UAV-BEHCHO-2017	0.55	2.59	0.79	3.19
UAV-PROVID-2017	0.59	2.69	1.07	3.35

measurements. The mean value and standard deviation (STD) of subsidence within barren land in both the entire interferogram and the common area were calculated from different interferograms.

Furthermore, we compared the four interferograms in three pairs (Table 3). Weighted linear fitting was conducted between each pair of InSAR observations. Equation 3 expresses the Cramer Rao bound on the variance of interferometric phase (σ_ϕ^2) which is weighted by coherence (γ) of each pixel (Werner et al., 2002). N_L is the number of looks of each interferogram. The variance of seasonal subsidence measurements (σ_S^2) is expressed in Equation 4 based on error propagation law. The weight of seasonal subsidence measurement (w) is calculated according to Equation 5.

$$\sigma_\phi^2 = \frac{1-\gamma^2}{\gamma^2}\frac{1}{2\times N_L} \tag{3}$$

$$\sigma_S^2 = \left(\frac{\lambda}{4\pi cos\theta} - \frac{\sqrt{ADDT_{max}}}{\sqrt{ADDT_2 - ADDT_1}}\right)^2 \sigma_\phi^2 \tag{4}$$

$$w = \frac{1}{\sigma_S^2} \tag{5}$$

Then the weighted mean bias, root mean square error (RMSE), and correlation coefficient (R) were calculated between each pair of measurements (Bailey et al., 2018).

Finally, the spatial patterns of the ALOS2 and UAVSAR InSAR results were compared and analyzed based on different landcover types by referring to the Canada landcover products version 2015. Thaw-season subsidence and coherence within needleleaf forest, taiga needleleaf forest, grassland, and shrubland observed from different InSAR measurements were also compared.

3. Results

3.1. Evaluation of Interferograms

Figure 4 shows subsidence maps generated from the ALOS2 and UAVSAR interferograms. Generally, the entire ALOS2-2017 interferogram is relatively homogeneous. The spatial patterns in the two UAVSAR interferograms are similar without significant spatial gaps or artifacts.

The STD of subsidence within barren land from different products are listed in Table 2. Figure 5 shows the histograms of subsidence in the barren land from the entire interferogram and the common area, respectively.

The distribution of subsidence in the barren land obtained from the satellite InSAR observations is concentrated in a narrow range. In contrast, the subsidence of barren land measured by UAVSAR exhibits a broader range of values. In addition, the STD of vertical displacement within the barren land estimated from the satellite interferograms are generally lower than the values of the BEHCHO and PROVID interferograms. In general, the UAVSAR results reflected apparent spatial subsidence variation in the barren regions that is not captured by the spaceborne observations.

In the ideal case, there is no deformation during the thaw season over barren land. But there is a 2-year interval between the reference landcover map and the InSAR measurement. It is possible that vegetation grew in some barren regions during this period. Furthermore, some barren land may experience subsidence due to the seasonal thawing of soil that is not underlain by permafrost. These subsidence variations might be captured by the UAVSAR observations, leading to larger bias and STD of subsidence within barren land.

Table 3
Differences (Bias, RMSE, R) Between InSAR Measurements

	Mean bias (cm)	RMSE (cm)	*R*
ALOS2-2017 versus UAV-BEHCHO-2017	0.38	1.94	0.41
ALOS2-2017 versus UAV-PROVID-2017	0.19	2.01	0.41
UAV-BEHCHO-2017 versus UAV-PROVID-2017	0.15	1.59	0.70

3.2. Comparison of UAVSAR and ALOS2 Measurements

UAVSAR and ALOS2 interferograms are compared in three pairs, with the quantitative indexes shown in Table 3 and the scatter plots shown in Figure 6. The two UAVSAR observations show agreement with a relatively smaller deviation and the largest correlation coefficient (0.70). While the scatter diagrams demonstrate that the UAVSAR and ALOS2 measurements are less consistent. The correlation coefficients between ALOS2-2017 and UAVSAR results are only 0.41. The largest bias and RMSE lie in the comparison between ALOS2-2017 and UAV-PROVID-2017, with the RMSE reaching 2.01 cm. This distinct difference may be attributable to the different error sources between airborne and satellite platforms.

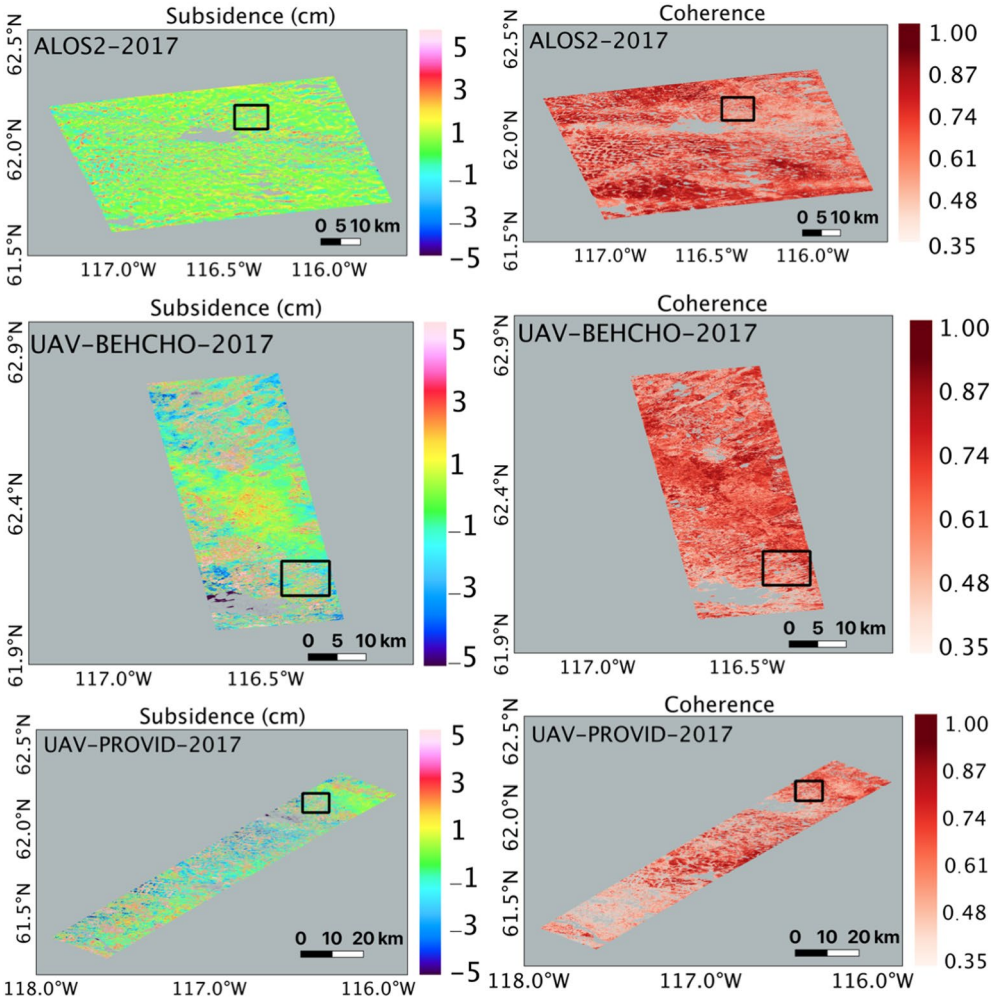

Figure 4. Subsidence map (left) and coherence map (right) of UAVSAR and ALOS2. The study area is outlined with black box. ALOS, Advanced Land Observing Satellite; UAVSAR, Uninhabited Aerial Vehicle Synthetic Aperture Radar.

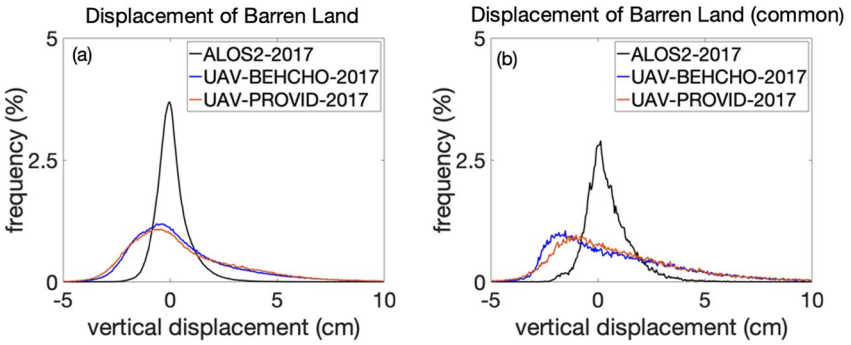

Figure 5. Histograms of subsidence in barren land derived from satellite and UAVSAR Interferograms (left) and common area (right). UAVSAR, Uninhabited Aerial Vehicle Synthetic Aperture Radar.

3.3. Spatial Pattern

Figure 7 shows the subsidence and coherence in the common study area. The spatial pattern corresponds most strongly with the various vegetation distribution.

The interferometric coherence indicates the quality of the InSAR results. Figure 7 suggests that the coherence of ALOS2 and UAVSAR observations are comparably high. According to Figure 8, the coherence of UAVSAR is slightly higher than the coherence of the ALOS2 interferograms in grassland types. In addition, Figure 9 shows that the coherence in grassland is slightly higher than other landcover types for both UAVSAR and ALOS2 interferograms, which indicates higher precision estimates of the deformation can be acquired over the grassland.

Both spaceborne and airborne interferograms demonstrated that the subsidence varies within different land cover types, and these patterns are more pronounced in the UAVSAR observations. Figure 10 indicates that the subsidence revealed by two UAVSAR interferograms agrees well in all four types of landcover. Our results show that the mean estimated thaw-season subsidence within taiga needleleaf-forest regions is generally larger than those in regions of needleleaf forest, shrubland, and grassland (Table 4). This phenomenon is evident in the UAVSAR interferograms. However, it is worth noting that the range of subsidence values observed from UAVSAR is larger than the range obtained from the ALOS2 measurement (Figure 11). The possible reasons for the difference may include the native resolution of the SAR scene, thermal noise from the antenna, misregistration, and the residual atmospheric effects. Even though the spatial resolution of the UAVSAR and ALOS2 subsidence map are both 30 m, the native resolution of L-band UAVSAR is 1.67 m in range and 0.6 m in azimuth, much finer than the resolution of ALOS2 SAR data (9.1 m in range × 5.3 m in azimuth). The UAVSAR measurements are potentially more sensitive to fine-scale variations in surface subsidence. Spaceborne InSAR with coarser spatial resolution tends to average these variations together, resulting in more concentrated observed subsidence values. The differences in surface subsidence among vegetation covers are possibly associated with wildfires, different microtopography, soil moisture, ALT,

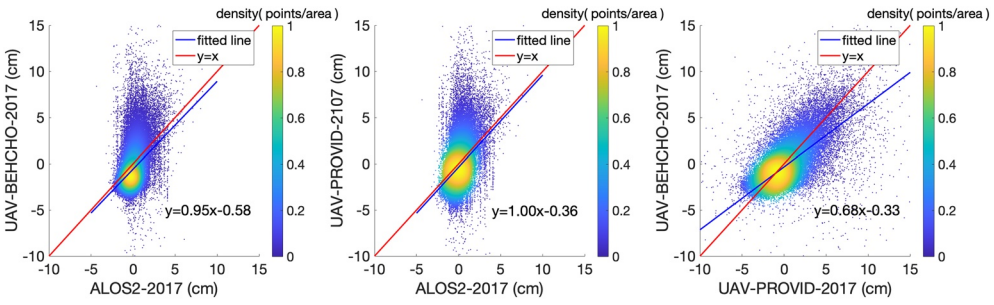

Figure 6. Scatter plot of vertical displacement of InSAR observations. In each panel, the red line is $y = x$ (1:1) and the blue line is the linear fit. InSAR, Interferometric Synthetic Aperture Radar.

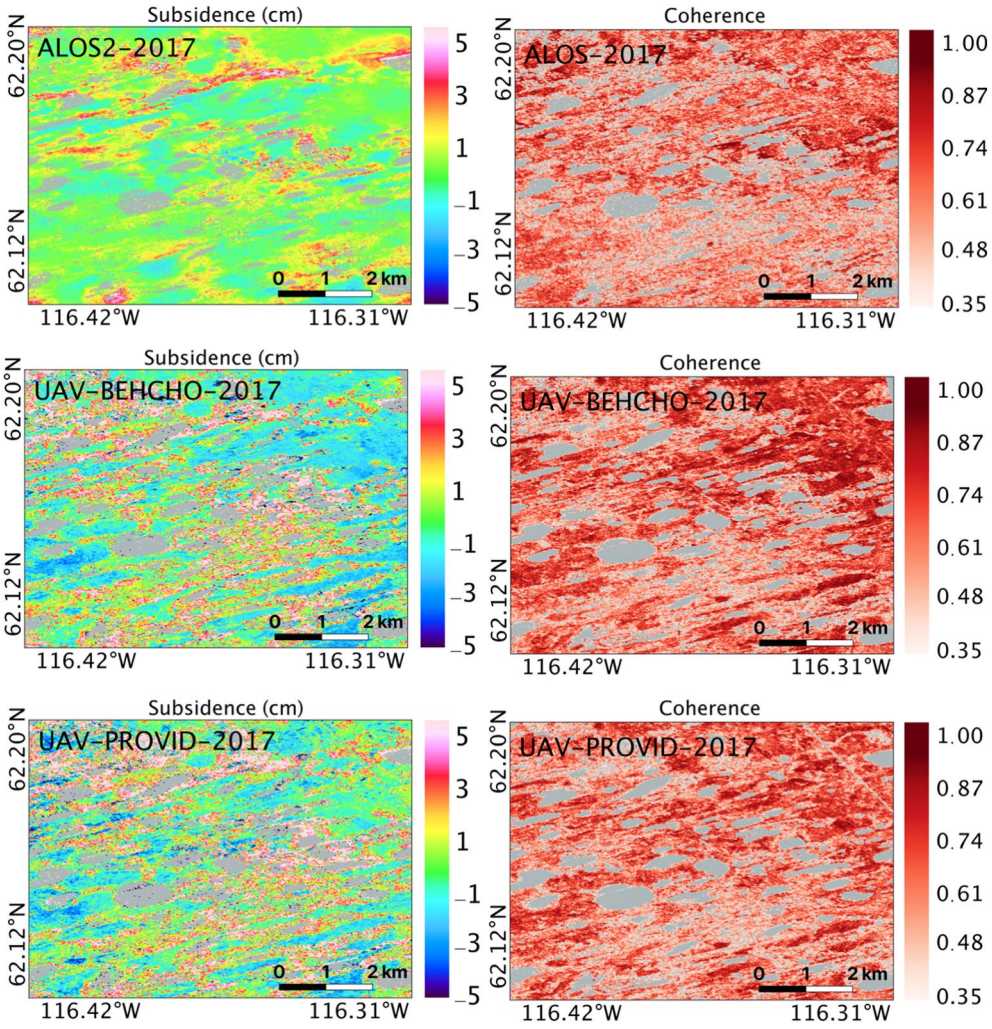

Figure 7. Subsidence (left) and corresponding coherence in the common area. Areas with coherence less than 0.35 are masked out.

organic content, and mineral content. This phenomenon and the underlying mechanisms need further investigation with subsidence reference and validation data obtained from ground-based measurements.

4. Discussion

4.1. Major Differences Between Spaceborne and Airborne InSAR Measurements

Interferograms generated from satellite and airborne InSAR data show different performances in quality and sensitivity in mapping surface subsidence. According to the comparison results, the subsidence derived from the two UAVSAR interferograms shows good agreement. The coherence of the UAVSAR interferograms is comparable with the coherence of the ALOS2 observations, and the former reveal more evident spatial subsidence variation in the study region. The correlation coefficients between the airborne UAVSAR and ALOS2 satellite results are low, and deviation (bias and RMSE) are relatively high. Therefore, it is possible that a systematic difference exists between the UAVSAR and ALOS2 results.

The large bias between the spaceborne and airborne InSAR results can be attributed to the notable differences between the two types of systems, such as employed instruments, imaging geometry, baseline estimation, and error sources. Since satellite imaging geometry is determined by the law of orbital mechanics, the spatial baseline of ALOS2 SAR imagery can be accurately estimated based on precision orbit data. On the

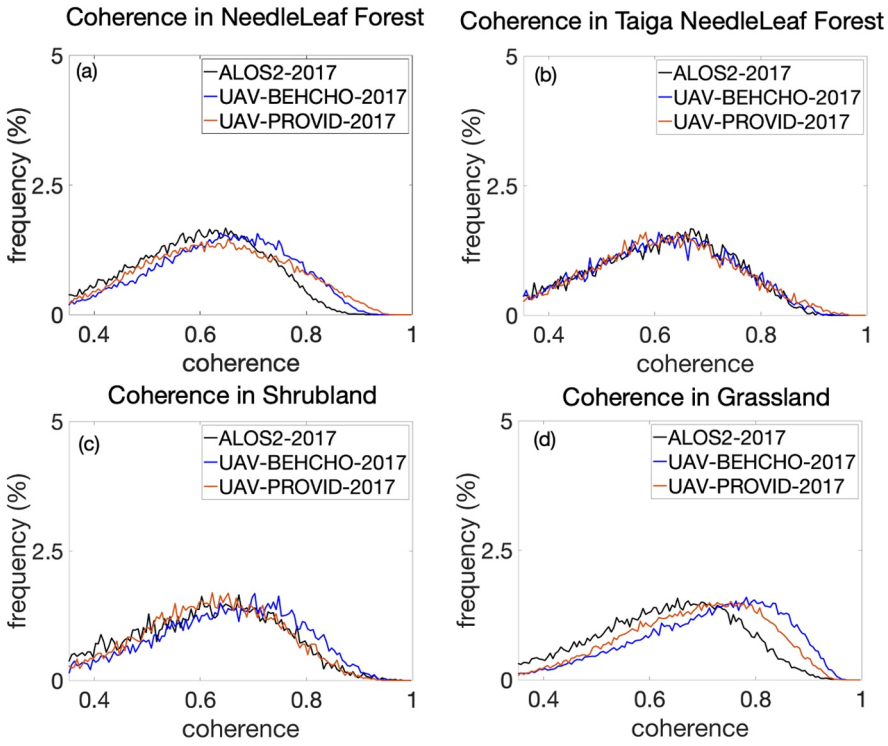

Figure 8. Histograms of coherence in various landcover regions.

contrary, the geometry configuration for UAVSAR can be adjusted according to observation scenarios (Cao et al., 2017). The baseline estimation for UAVSAR involving residual correction is more complicated than satellite InSAR. Aircraft motion caused by air turbulence should be a major factor influencing the accuracy of airborne InSAR observations. Compared with spaceborne SAR, incidence angle variation along the range direction is significantly larger in airborne SAR systems, for example, reaching approximately 40° in BEHCHO and PROVID swaths. The high pass box filter helps remove the large-scale propagational phase errors caused by tropospheric delay and aircraft positioning. But unmitigated aircraft motion and incidence angle variations may still result in small-scale subsidence effects in the final interferogram. Even after applying motion compensation, residual motion error still exists and could cause erroneous phase undulations in the UAVSAR data result. Hensley, Michel, et al. (2009) and Hensley, Zebker, et al. (2009) improved the residual motion estimation accuracy from 2 to 15 cm to the millimeter level (Hensley, Michel, et al., 2009; Hensley, Zebker, et al., 2009). From the perspective of error source, satellite observations suffer from ionospheric disturbance due to the spatial and temporal variation of electrons in the ionosphere (Wegmuller et al., 2006). While the radar signal of the airborne instrument only experiences tropospheric water vapor delay without propagating through the ionosphere.

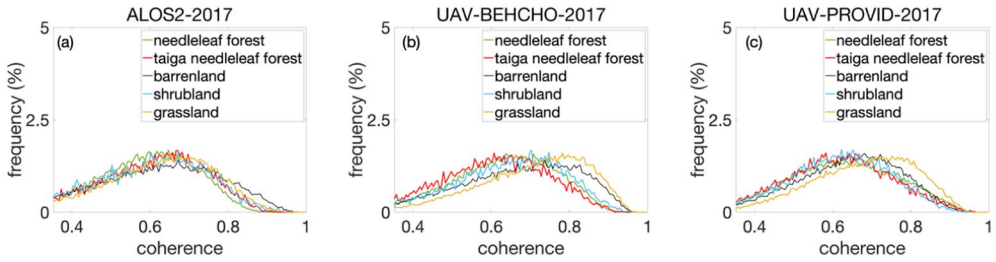

Figure 9. Histograms of coherence in different interferograms.

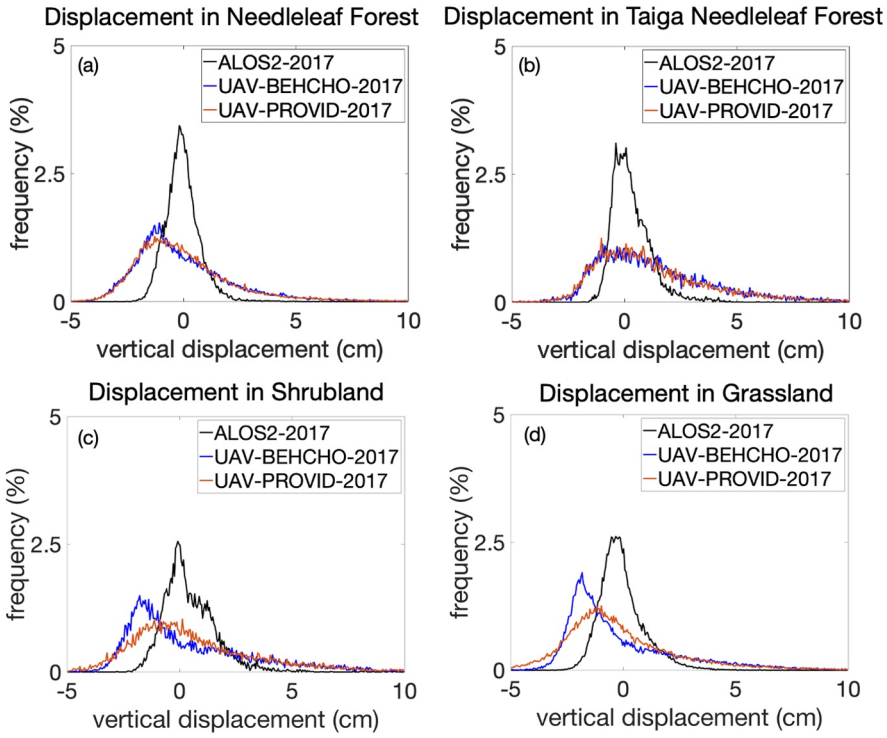

Figure 10. Histograms of vertical displacement in various landcover regions.

In terms of spatial patterns, UAVSAR observations are able to reveal a distinct difference in surface subsidence within various vegetation types. The larger spread in subsidence values, as well as the subtle features observed by UAVSAR are possibly attributed to the finer native resolution of the UAVSAR compared to the ALOS2 measurements. With a range bandwidth of 80 MHz, UAVSAR radar provides single-look complex data at 1.67 m in range and 0.6 m in azimuth. While the resolution of ALOS2 data products (9.1 m range, 5.3 m azimuth) are one order of magnitude coarser than airborne data. The InSAR-derived subsidence maps demonstrate that UAVSAR interferograms are able to capture fine-scale spatial heterogeneity of permafrost subsidence. With degrading spatial resolution, the subsidence map derived from ALOS2 is relatively uniform and the measured spatial variability in surface subsidence is not as high as in the UAVSAR results. The histograms of vertical displacements in different interferograms also show that the ALOS2 measured subsidence is distributed in a narrow range. The subsidence within various vegetation types is consistent. In contrast, the deviations in subsidence between different landcover are observed from the UAVSAR measurements. The finer native resolution makes the UAVSAR results reveal fine-scale spatial variability across the permafrost environments. If this phenomenon is further validated with the aid of ground-based data such as surface elevation change, ALT, and soil moisture, the capability of UAVSAR interferograms to identify fine-scale subsidence patterns could be utilized for precision measurements in permafrost areas. In addition, the biases between UAVSAR and ALOS2 InSAR results could be possibly corrected with reliable elevation change data obtained from in-situ measurements such as benchmark, leveling, tile arm (Gruber, 2020; Harris et al., 2007; Mackay & Leslie, 1987), or GPS interferometric reflectometry observations (Hu et al., 2018).

Table 4
Statistical Mean (cm) and Standard Deviation (cm) of Thaw-Season Subsidence for Different Types of Landcover

	Needleleaf		Shrubland		Grassland		Taiga needleleaf	
Interferogram-ID	Mean	STD	Mean	STD	Mean	STD	Mean	STD
ALOS2-2017	−0.04	0.76	0.46	1.22	−0.06	1.01	0.30	0.87
UAV-BEHCHO-2017	−0.02	2.30	0.50	3.12	−0.09	2.70	1.40	2.83
UAV-PROVID-2017	0.02	2.43	0.78	3.37	−0.09	2.73	1.37	3.03

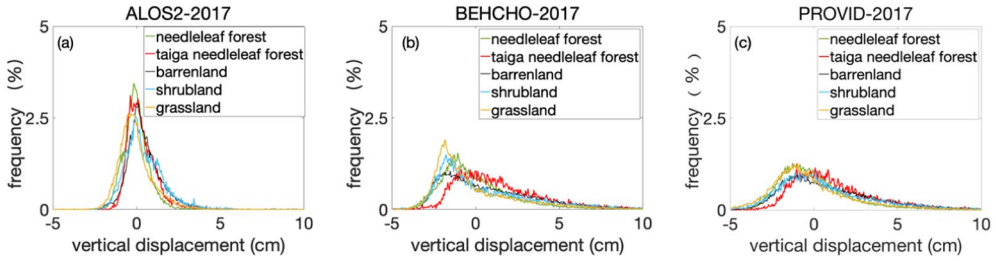

Figure 11. Histograms of vertical displacement in different interferograms.

4.2. How to Integrate Spaceborne and Airborne Measurements

Compared with satellite InSAR, airborne InSAR measurements have the characteristics of flexible revisit time and higher spatial resolution. These advantages can be utilized to improve the subsidence measurements by combining UAVSAR and remote sensing InSAR techniques.

Satellite InSAR and UAVSAR observations could be combined in the aspect of space since they have different spatial resolutions and coverage. The fine native resolution of UAVSAR allows the measurements to capture fine-scale spatial heterogeneity. UAVSAR observations characterize subtle features of subsidence at local scales, and satellite InSAR measurements provide observations with broader spatial coverage. Airborne UAVSAR measurements could be integrated with satellite observations to help to characterize detailed spatial patterns of subsidence over large permafrost regions.

In addition, UAVSAR and ALOS2 observations characterize the surface elevation movement with different time intervals, which could be integrated to estimate seasonal subsidence with higher accuracy over permafrost regions. More observations in the thaw season help to reduce uncertainties in estimating whole-season subsidence and enable quantification of the temporal evolution of permafrost.

The seasonal subsidence could be estimated with three different observation scenarios as in the conceptual plan illustrated in Figure 12.

In the first scenario, only the spaceborne InSAR observations (τ1 and τ2 in Figure 12) are available and used to estimate seasonal subsidence. Satellite measurements are at regular monthly intervals(or sub-monthly, even weekly, depending on satellite missions) and are possibly acquired in the middle of the thawing season. In this case, seasonal scaling is required to extrapolate short-span interferograms to derive the net seasonal subsidence, which may introduce additional errors by multiplying the scaling factor (α). The uncertainty of estimated seasonal subsidence can be expressed in Equation 6.

$$\varepsilon_s = \left[\left(\frac{\partial S}{\partial D} \varepsilon_D \right)^2 + \left(\frac{\partial S}{\partial ADDT_{max}} \varepsilon_{ADDT_{max}} \right)^2 + \left(\frac{\partial S}{\partial ADDT_2} \varepsilon_{ADDT_2} \right)^2 + \left(\frac{\partial S}{\partial ADDT_1} \varepsilon_{ADDT_1} \right)^2 \right]^{\frac{1}{2}} \quad (6)$$

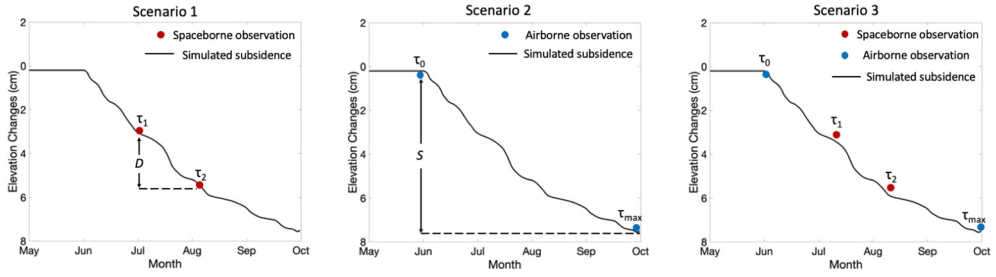

Figure 12. Conceptual scheme illustrates a way to combine airborne and spaceborne InSAR observations in estimating seasonal subsidence. InSAR, Interferometric Synthetic Aperture Radar.

Table 5
Associated Parameters and Uncertainties for Spaceborne Measurement

	α	εD(cm)	εs(cm)
ALOS2-2017	1.43	0.58	0.83

Taking the ALOS2 measurements as an example, the temperature uncertainty is small and can be ignored. And the uncertainty of vertical displacement measurement is represented by the STD of vertical displacement in all barren land pixels in a certain interferogram. Then the uncertainty of measuring the seasonal subsidence from ALOS2 InSAR observations is shown in Table 5. The seasonal scaling methods utilized also introduce uncertainties and even biases into the estimation of seasonal subsidence. Therefore, the seasonal subsidence in a permafrost area cannot be accurately captured by spaceborne measurements due to the regular yet sparse time sampling.

In the second scenario, UAVSAR measurements are the only available observations. Airborne platforms can offer SAR observations with the flexibility of the revisit operation time. If the UAVSAR measurements are conducted at the beginning and the end of the thaw season (τ_0 and τ_{max} in Figure 12), the total seasonal subsidence (s) of the permafrost can be obtained without seasonal scaling, and the corresponding uncertainty of estimated seasonal subsidence equals the uncertainty of vertical displacement.

Third, if both remote sensing and airborne UAVSAR measurements are available during the thaw season, these two types of InSAR measurements can be utilized to precisely characterize the trend of the surface elevation change with high-temporal resolution observations available. A combination of airborne and satellite InSAR results provides a better description of subsidence evolution during the thaw season.

5. Conclusions

In this study, we produced ALOS2 and UAVSAR interferograms and generated subsidence maps over a permafrost area located near Yellowknife, Canada. These interferograms show different performances in quality, coherence, and sensitivity in characterizing ground subsidence. The coherence of ALOS2 and UAVSAR interferograms are comparable. The subsidence derived from the two UAVSAR interferograms is in good agreement, while a distinct difference exists between the UAVSAR and ALOS2 results with the RMSE around 2 cm and the correlation coefficients lower than 0.5. In addition, both the ALOS2 and UAVSAR results show different subsidence within the various land cover types in the study area.

We observed existing systematic differences between the UAVSAR and ALOS2 observations of surface subsidence across the permafrost region. The deviations between airborne and spaceborne measurements are possibly attributed to different native spatial resolution, error sources, and processing procedures. The flexible observation intervals and finer resolution of UAVSAR data sets encourage us to make use of growing airborne InSAR measurements for improved characterization of subsidence evolution over large permafrost regions. Nevertheless, the systematic difference is a necessary factor that needs to be considered before merging the remote detection of permafrost subsidence derived from airborne and spaceborne platforms. Airborne and spaceborne InSAR data sets have the potential to be integrated for accurate estimates of thaw-season subsidence across permafrost regions when future SAR missions such as NISAR or ROSE-L are operational.

Data Availability Statement

The ALOS2 data for this research are copyrighted by the Japan Aerospace Exploration Agency (JAXA) and provided through the EO-RA2 project ER2A2N081. The raw ALOS2 data used in this research are stored online (https://zenodo.org/record/4429635). The two UAVSAR interferograms (BEHCHO & PROVID) are processed and published by NASA Jet Propulsion Laboratory (JPL) and available online (UAVSAR-BEHCHO: http://uavsar.jpl.nasa.gov/cgi-bin/product.pl?jobName=behcho_35302_17063-007_17094-007_0087d_s01_L090_01 and UAVSAR-PROVID: http://uavsar.jpl.nasa.gov/cgi-bin/product.pl?jobName=provid_04006_17063-006_17094-006_0087d_s01_L090_01). The 2015 land cover of Canada are published by the Government of Canada and are available from https://open.canada.ca/data/en/dataset/4e615eae-b90c-420b-adee-2ca35896caf6. These data are stored online (https://zenodo.org/record/4429635).

Acknowledgments
Great thanks to editors and two reviewers for their constructive suggestions and insightful comments. This study is supported by the following funders: the Hong Kong Research Grants Council (CUHK 14303119 and HKPFS PF18-21555), and NASA Grant NNX17AC59A.

References

Antonova, S., Sudhaus, H., Strozzi, T., Zwieback, S., Kääb, A., Heim, B., et al. (2018). Thaw subsidence of a Yedoma landscape in northern Siberia, measured in situ and estimated from TerraSAR-X interferometry. *Remote Sensing*, *10*(4), 494. https://doi.org/10.3390/rs10040494

Bailey, P., Emad, A., Zhang, T., Xie, Q., & Sikali, E. (2018). *Weighted and unweighted correlation methods for large-scale educational assessment: wCorr formulas*. (AIR--NAEP Working Paper No. 2018-01. NCES Data R Project Series# 02). American Institutes for Research.

Bardi, F., Frodella, W., Ciampalini, A., Bianchini, S., Del Ventisette, C., Gigli, G., et al. (2014). Integration between ground based and satellite SAR data in landslide mapping: The San Fratello case study. *Geomorphology*, *223*, 45–60. https://doi.org/10.1016/j.geomorph.2014.06.025

Beamish, A., Raynolds, M. K., Epstein, H., Frost, G. V., Macander, M. J., Bergstedt, H., et al. (2020). Recent trends and remaining challenges for optical remote sensing of Arctic tundra vegetation: A review and outlook. *Remote Sensing of Environment*, *246*, 111872. https://doi.org/10.1016/j.rse.2020.111872

Beck, I., Ludwig, R., Bernier, M., Strozzi, T., & Boike, J. (2015). Vertical movements of frost mounds in subarctic permafrost regions analyzed using geodetic survey and satellite interferometry. *Earth Surface Dynamics*, *3*(3), 409–421. https://doi.org/10.5194/esurf-3-409-2015

Brcic, R., Parizzi, A., Eineder, M., Bamler, R., & Meyer, F. (2010). Estimation and compensation of ionospheric delay for SAR interferometry. In *Paper presented at the 2010 IEEE International Geoscience and Remote Sensing Symposium* (pp. 2908–2911). IEEE.

Brown, D. R., Jorgenson, M. T., Douglas, T. A., Romanovsky, V. E., Kielland, K., Hiemstra, C., et al. (2015). Interactive effects of wildfire and climate on permafrost degradation in Alaskan lowland forests. *Journal of Geophysical Research: Biogeosciences*, *120*(8), 1619–1637. https://doi.org/10.1002/2015jg003033

Cao, N., Lee, H., Zaugg, E., Shrestha, R., Carter, W., Glennie, C., et al. (2017). Airborne DInSAR results using time-domain Backprojection algorithm: A case study over the Slumgullion Landslide in Colorado with validation using Spaceborne SAR, Airborne LiDAR, and ground-based observations. *IEEE Journal of Selected Topics in Applied Earth Observations and Remote Sensing*, *10*(11), 4987–5000. https://doi.org/10.1109/jstars.2017.2737362

Carlà, T., Farina, P., Intrieri, E., Ketizmen, H., & Casagli, N. (2018). Integration of ground-based radar and satellite InSAR data for the analysis of an unexpected slope failure in an open-pit mine. *Engineering Geology*, *235*, 39–52. https://doi.org/10.1016/j.enggeo.2018.01.021

Carlà, T., Tofani, V., Lombardi, L., Raspini, F., Bianchini, S., Bertolo, D., et al. (2019). Combination of GNSS, satellite InSAR, and GBInSAR remote sensing monitoring to improve the understanding of a large landslide in high alpine environment. *Geomorphology*, *335*, 62–75. https://doi.org/10.1016/j.geomorph.2019.03.014

Chen, C. W., & Zebker, H. A. (2002). Phase unwrapping for large SAR interferograms: Statistical segmentation and generalized network models. *IEEE Transactions on Geoscience and Remote Sensing*, *40*(8), 1709–1719. https://doi.org/10.1109/tgrs.2002.802453

Chen, J., Liu, L., Zhang, T., Cao, B., & Lin, H. (2018). Using persistent scatterer interferometry to map and quantify permafrost thaw subsidence: A case study of Eboling Mountain on the Qinghai-Tibet Plateau. *Journal of Geophysical Research: Earth Surface*, *123*(10), 2663–2676. https://doi.org/10.1029/2018jf004618

Chen, R. H., Tabatabaeenejad, A., & Moghaddam, M. (2019). Retrieval of permafrost active layer properties using time-series P-band radar observations. *IEEE Transactions on Geoscience and Remote Sensing*, *57*(8), 6037–6054. https://doi.org/10.1109/tgrs.2019.2903935

Daout, S., Doin, M. P., Peltzer, G., Socquet, A., & Lasserre, C. (2017). Large-scale InSAR monitoring of permafrost freeze-thaw cycles on the Tibetan Plateau. *Geophysical Research Letters*, *44*(2), 901–909. https://doi.org/10.1002/2016gl070781

Delbridge, B. G., Bürgmann, R., Fielding, E., & Hensley, S. (2015). Kinematics of the slumgullion landslide from UAVSAR derived interferograms. In *Paper presented at the 2015 IEEE International Geoscience and Remote Sensing Symposium (IGARSS)* (pp. 3842–3845). IEEE.

Delbridge, B. G., Bürgmann, R., Fielding, E., Hensley, S., & Schulz, W. H. (2016). Three-dimensional surface deformation derived from airborne interferometric UAVSAR: Application to the Slumgullion Landslide. *Journal of Geophysical Research: Solid Earth*, *121*(5), 3951–3977. https://doi.org/10.1002/2015jb012559

Donnellan, A., Parker, J., Hensley, S., Pierce, M., Wang, J., & Rundle, J. (2014). UAVSAR observations of triggered slip on the Imperial, Superstition Hills, and East Elmore Ranch Faults associated with the 2010 M 7.2 El Mayor-Cucapah earthquake. *Geochemistry, Geophysics, Geosystems*, *15*(3), 815–829. https://doi.org/10.1002/2013gc005120

Duncan, B. N., Ott, L. E., Abshire, J. B., Brucker, L., Carroll, M. L., Carton, J., et al. (2020). Space-based observations for understanding changes in the Arctic-Boreal Zone. *Reviews of Geophysics*, *58*(1), e2019RG000652. https://doi.org/10.1029/2019rg000652

Fattahi, H., Simons, M., & Agram, P. (2017). InSAR time-series estimation of the ionospheric phase delay: An extension of the split range-spectrum technique. *IEEE Transactions on Geoscience and Remote Sensing*, *55*(10), 5984–5996. https://doi.org/10.1109/tgrs.2017.2718566

Fielding, E. J., Handwerger, A. L., Burgmann, R., & Liu, Z. (2017). Slow, fast, and post-collapse displacements of the Mud Creek landslide in California from UAVSAR and satellite SAR analysis. In *Paper presented at the AGU Fall Meeting Abstracts*.

Gomba, G., Parizzi, A., De Zan, F., Eineder, M., & Bamler, R. (2015). Toward operational compensation of ionospheric effects in SAR interferograms: The split-spectrum method. *IEEE Transactions on Geoscience and Remote Sensing*, *54*(3), 1446–1461.

Gruber, S. (2020). Ground subsidence and heave over permafrost: Hourly time series reveal interannual, seasonal and shorter-term movement caused by freezing, thawing and water movement. *The Cryosphere*, *14*(4), 1437–1447. https://doi.org/10.5194/tc-14-1437-2020

Harris, C., Luetschg, M., Davies, M. C., Smith, F., Christiansen, H. H., & Isaksen, K. (2007). Field instrumentation for real-time monitoring of periglacial solifluction. *Permafrost and Periglacial Processes*, *18*(1), 105–114. https://doi.org/10.1002/ppp.573

Hensley, S., Michel, T., Simard, M., Jones, C., Muellerschoen, R., Le, C., et al. (2009). Residual motion estimation for UAVSAR: Implications of an electronically scanned array. In *Paper presented at the 2009 IEEE Radar Conference* (pp. 1–5). IEEE.

Hensley, S., Zebker, H., Jones, C., Michel, T., Muellerschoen, R., & Chapman, B. (2009). First deformation results using the NASA/JPL UAVSAR instrument. In *Paper presented at the 2009 2nd Asian-Pacific Conference on Synthetic Aperture Radar* (pp. 1051–1055). IEEE.

Hjort, J., Karjalainen, O., Aalto, J., Westermann, S., Romanovsky, V. E., Nelson, F. E., & Luoto, M. (2018). Degrading permafrost puts Arctic infrastructure at risk by mid-century. *Nature Communications*, *9*(1), 1–9. https://doi.org/10.1038/s41467-018-07557-4

Hu, Y., Liu, L., Larson, K. M., Schaefer, K. M., Zhang, J., & Yao, Y. (2018). GPS interferometric reflectometry reveals cyclic elevation changes in thaw and freezing seasons in a permafrost area (Barrow, Alaska). *Geophysical Research Letters*, *45*(11), 5581–5589. https://doi.org/10.1029/2018gl077960

Liu, L., Schaefer, K., Zhang, T., & Wahr, J. (2012). Estimating 1992–2000 average active layer thickness on the Alaskan North Slope from remotely sensed surface subsidence. *Journal of Geophysical Research: Earth Surface*, *117*(F1), F01005. https://doi.org/10.1029/2011jf002041

Liu, L., Zhang, T., & Wahr, J. (2010). InSAR measurements of surface subsidence over permafrost on the North Slope of Alaska. *Journal of Geophysical Research: Earth Surface*, *115*(F3), F03023. https://doi.org/10.1029/2009jf001547

Mackay, J. R. (1995). Active layer changes (1968 to 1993) following the forest-tundra fire near Inuvik, NWT, Canada. *Arctic and Alpine Research*, *27*(4), 323–336. https://doi.org/10.2307/1552025

Mackay, J. R., & Burn, C. R. (2002). The first 20 years (1978-1979 to 1998-1999) of active-layer development, Illisarvik experimental drained lake site, western Arctic coast, Canada1. *Canadian Journal of Earth Sciences*, *39*(11), 1657–1674. https://doi.org/10.1139/e02-068

Mackay, J. R., & Leslie, R. V. (1987). A simple probe for the measurement of frost heave within frozen ground in a permafrost environment. *Current Research, Part A Geological Survey of Canada*, 37–41. https://doi.org/10.4095/122503

Michaelides, R., Chen, R. Z. Y., Schaefer, K., Parsekian, A., Sullivan, P., Moghaddam, M., et al. (2021). Permafrost Dynamics Observatory (PDO) – Part I: Postprocessing and Calibration Methods of UAVSAR L-band InSAR Data for Seasonal Subsidence Estimation. *Earth Space Science*. https://earthandspacescience-submit.agu.org/cgi-bin/main.plex?form_type=status_details&j_id=476&ms_id=897742&ms_rev_no=1&ms_id_key=ftdfeYHNDfWPCgkHSO71niuKw

Michaelides, R., Schaefer, K., Zebker, H., Parsekian, A., Liu, L., Chen, J., & Schaefer, S. (2019). Inference of the impact of wildfire on permafrost and active layer thickness in a discontinuous permafrost region using the remotely sensed active layer thickness (ReSALT) algorithm. *Environmental Research Letters*, *14*, 035007.

Miller, C. E., Griffith, P. C., Goetz, S. J., Hoy, E. E., Pinto, N., McCubbin, I. B., et al. (2019). An overview of ABoVE airborne campaign data acquisitions and science opportunities. *Environmental Research Letters*, *14*(8), 080201. https://doi.org/10.1088/1748-9326/ab0d44

Nauta, A. L., Heijmans, M. M., Blok, D., Limpens, J., Elberling, B., Gallagher, A., et al. (2015). Permafrost collapse after shrub removal shifts tundra ecosystem to a methane source. *Nature Climate Change*, *5*(1), 67–70. https://doi.org/10.1038/nclimate2446

Rosen, P. A., Gurrola, E., Sacco, G. F., & Zebker, H. (2012). The InSAR scientific computing environment. In *Paper presented at the EUSAR 2012; 9th European Conference on Synthetic Aperture Radar* (pp. 730–733). VDE .

Rosen, P. A., Hensley, S., & Chen, C. (2010). Measurement and mitigation of the ionosphere in L-band interferometric SAR data. In *Paper presented at the 2010 IEEE Radar Conference* (pp. 1459–1463). IEEE.

Schaefer, K., Liu, L., Parsekian, A., Jafarov, E., Chen, A., Zhang, T., et al. (2015). Remotely sensed active layer thickness (ReSALT) at Barrow, Alaska using interferometric synthetic aperture radar. *Remote Sensing*, *7*(4), 3735–3759. https://doi.org/10.3390/rs70403735

Schaefer, L. N., Lu, Z., & Oommen, T. (2015). Dramatic volcanic instability revealed by InSAR. *Geology*, *43*(8), 743–746. https://doi.org/10.1130/g36678.1

Schaefer, L. N., Lu, Z., & Oommen, T. (2016). Post-eruption deformation processes measured using ALOS-1 and UAVSAR InSAR at Pacaya Volcano, Guatemala. *Remote Sensing*, *8*(1), 73. https://doi.org/10.3390/rs8010073

Schuur, E. A., McGuire, A. D., Schädel, C., Grosse, G., Harden, J. W., Hayes, D. J., et al. (2015). Climate change and the permafrost carbon feedback. *Nature*, *520*(7546), 171–179. https://doi.org/10.1038/nature14338

Short, N., Brisco, B., Couture, N., Pollard, W., Murnaghan, K., & Budkewitsch, P. (2011). A comparison of TerraSAR-X, RADARSAT-2 and ALOS-PALSAR interferometry for monitoring permafrost environments, case study from Herschel Island, Canada. *Remote Sensing of Environment*, *115*(12), 3491–3506. https://doi.org/10.1016/j.rse.2011.08.012

Shur, Y. L., & Jorgenson, M. T. (2007). Patterns of permafrost formation and degradation in relation to climate and ecosystems. *Permafrost and Periglacial Processes*, *18*(1), 7–19. https://doi.org/10.1002/ppp.582

Stefan, J. (1891). Über die Theorie der Eisbildung, insbesondere über die Eisbildung im Polarmeere. *Annalen der Physik und Chemie*, *42*, 269–286. https://doi.org/10.1002/andp.18912780206

Stevens, D. R., Cumming, I. G., & Gray, A. L. (1995). Options for airborne interferometric SAR motion compensation. *IEEE Transactions on Geoscience and Remote Sensing*, *33*(2), 409–420. https://doi.org/10.1109/36.377941

Streletskiy, D. A., Shiklomanov, N. I., Little, J. D., Nelson, F. E., Brown, J., Nyland, K. E., & Klene, A. E. (2017). Thaw subsidence in undisturbed tundra landscapes, Barrow, Alaska, 1962–2015. *Permafrost and Periglacial Processes*, *28*(3), 566–572. https://doi.org/10.1002/ppp.1918

Strozzi, T., Antonova, S., Günther, F., Mätzler, E., Vieira, G., Wegmüller, U., et al. (2018). Sentinel-1 SAR interferometry for surface deformation monitoring in low-land permafrost areas. *Remote Sensing*, *10*(9), 1360. https://doi.org/10.3390/rs10091360

Turetsky, M. R., Abbott, B. W., Jones, M. C., Anthony, K. W., Olefeldt, D., Schuur, E. A., et al. (2020). Carbon release through abrupt permafrost thaw. *Nature Geoscience*, *13*(2), 138–143. https://doi.org/10.1038/s41561-019-0526-0

Wang, L., Marzahn, P., Bernier, M., Jacome, A., Poulin, J., & Ludwig, R. (2017). Comparison of TerraSAR-X and ALOS PALSAR differential interferometry with multisource DEMs for monitoring ground displacement in a discontinuous permafrost region. *IEEE Journal of Selected Topics in Applied Earth Observations and Remote Sensing*, *10*(9), 4074–4093. https://doi.org/10.1109/jstars.2017.2707337

Wegmuller, U., Werner, C., Strozzi, T., & Wiesmann, A. (2006). Ionospheric electron concentration effects on SAR and INSAR. In *Paper presented at the 2006 IEEE International Symposium on Geoscience and Remote Sensing* (pp. 3731–3734). IEEE.

Werner, C., Wegmüller, U., Strozzi, T., & Wiesmann, A. (2002). Processing strategies for phase unwrapping for INSAR applications. In *Paper presented at the European Conference on Synthetic Aperture Radar EUSAR*.